Networks and Heterogeneous Media

https://www.aimspress.com/journal/nhm

NHM, 21(2): 402–425.
DOI: 10.3934/nhm.2026019
Received: 28 January 2026
Revised: 09 March 2026
Accepted: 16 March 2026
Published: 24 March 2026

Research article

An efficient adaptive moving grid algorithm for time-fractional integrodifferential equations governing viscoelastic nanofluid dynamics

Zhi Mao[1,2], Huafang Li[2], Xiaobing Bao[3],* Leilei Wei[4],* Libin Liu[5] and Libo Feng[6]

[1] School of Data Science, Tongren University, Tongren 554300, China

[2] School of Mathematics and Statistics, Jishou University, Xiangxi 416100, China

[3] School of Big Data and Artificial Intelligence, Chizhou University, Chizhou 247000, China

[4] School of Mathematics and Statistics, Henan University of Technology, Zhengzhou 450001, China

[5] School of Mathematics and Statistics, Nanning Normal University, Nanning 530100, China

[6] School of Mathematical Sciences, Queensland University of Technology, GPO Box 2434, Brisbane, Qld. 4001, Australia

* **Correspondence:** Email: czubxb@163.com, leileiwei@haut.edu.cn.

Abstract: An adaptive moving grid method is developed to solve the time-fractional integrodifferential governing equations of viscoelastic nanofluid. The momentum equation is derived based on a dual-parameter fractional Maxwell constitutive relation, and the energy equation employs a generalized Cattaneo heat conduction relation. To improve solution accuracy, a monitor function based on the equidistribution principle is constructed, and an adaptive mesh redistribution strategy is developed in the spatial domain. The temporal fractional-order operators are approximated by the L1 algorithm and the weighted-shifted Grünwald difference method. Numerical experiments demonstrate that the adaptive grid achieves 77.6–88.4% higher accuracy compared to uniform grids at the same grid scale, along with enhanced stability in convergence. Parametric analysis indicates that increasing the fractional-order derivative in the energy equation results in a thickening of both the velocity and thermal boundary layers. Furthermore, the dual-fractional Maxwell model exhibits a thicker velocity boundary layer than its classical single-parameter counterpart. The proposed method offers an efficient and robust approach for simulating complex viscoelastic nanofluid systems with memory effects and multi-field coupling.

Keywords: adaptive moving grid; fractional integrodifferential equations; viscoelastic nanofluid; fractional Maxwell model; generalized Cattaneo heat conduction relation

1. Introduction

Viscoelastic fluids, as a subclass of non-Newtonian fluids, are widely encountered in numerous industrial applications, such as cosmetics, polymer manufacturing, coatings, printing technologies, biological systems, and so forth [1]. These materials exhibit complex rheological behaviors due to the nonlinear stress–strain relationship [2]. To accurately capture their memory-dependent behavior, classical viscoelastic models (e.g., Maxwell, Oldroyd-B, and Jeffreys models) have been effectively generalized using fractional calculus [3–6]. This development has significantly promoted the modeling of viscoelastic fluids and improved the understanding of their heat and mass transfer mechanisms. For instance, Zhao et al. [7] established fractional boundary layer equations for viscoelastic fluids by incorporating a fractional Maxwell constitutive model across a vertical plate. Liu et al. [8] investigated laminar boundary-layer flow using a distributed-order time-fractional Maxwell model. Feng et al. [9] introduced a fractional Kelvin–Voigt constitutive relation to systematically derive the temperature boundary layer equations for nanofluids.

Optimizing convective heat transfer is a critical requirement in industry. Newtonian heating, owing to its exceptional heat transfer characteristics, has attracted increasing attention in petroleum engineering, energy systems, and mechanical processes [10]. Additionally, Newtonian heating has been introduced into the study of convective heat transfer of nanofluids. Aleem et al. [11] examined the unsteady magnetohydrodynamic nanofluid flow through a porous medium with an accelerating vertical plate, accounting for Newtonian heating and chemical reaction effects. Mao et al. [12] derived fractional integrodifferential governing equations using a dual-parameter fractional Maxwell model to investigate transient, free convection of viscoelastic nanofluids subject to Newtonian heating. The Newtonian heating boundary condition is classified as a Robin boundary condition in heat transfer analysis, which leads the solutions to exhibit singular perturbation behavior in the boundary layer. Classical numerical methods employing a uniform mesh cannot adequately resolve the sharp gradients within the boundary layer, leading to solution inaccuracies and numerical instability, especially for long-term simulations.

In recent years, considerable attention has also been devoted to the development of analytical and numerical techniques for fractional differential equations arising in complex physical systems. Various semianalytical and computational approaches have been proposed to investigate nonlinear fractional models, including the homotopy-based method [13–15], the perturbation technique [16], the finite difference method [17, 18], the finite element method [19], and the spectral method [20]. Nevertheless, accurately capturing the dynamics of boundary layers with sharp gradients requires robust numerical schemes to ensure reliable solutions. This characteristic necessitates the use of nonuniform grids to locally refine regions where the solution exhibits sharp variations. Nonuniform grids, as a useful tool for improving computational efficiency and accuracy, have been studied in fluid mechanics and heat transfer problems [21–23]. Early methods, such as algebraic grids [24], optimized the discretization by statically refining high-gradient regions, but they rely on prior information of the solution behavior within the boundary layer. In contrast, adaptive grid methods dynamically adjust mesh density based on the evolving solution, providing enhanced flexibility and accuracy. In recent years, adaptive grids have demonstrated significant advantages in numerically solving singular perturbation problems (see, e.g., [25–28]). Mao et al. [29] developed a robust adaptive grid method to solve singularly perturbed Fredholm integrodifferential equations, utilizing a posterior error estimation and mesh equidistribution principles. However, few studies have employed adaptive moving grid methods to solve the boundary

layer governing equations of nanofluids. Motivated by the adaptive grid method for singularly perturbed convection–diffusion systems with Robin boundary conditions [30] and the adaptive mesh strategy for unsteady nanofluid heat transfer [31], this study develops an adaptive grid algorithm based on the equidistribution principle to solve fractional integrodifferential equations of viscoelastic fluids.

In many practical applications, the surface heat flux varies linearly with the local temperature, corresponding to the Newtonian heating condition. Building on the above studies, this work examines the transient, free convective flow of incompressible nanofluids along a vertical infinite plate under Newtonian heating and thermal radiation. The constructed fractional integrodifferential equations for viscoelastic nanofluid flow are solved numerically on an adaptive moving grid. The main novel contributions of this work are as follows:

- An adaptive moving grid method based on the equidistribution principle is developed to solve the time-fractional integrodifferential boundary layer equations of viscoelastic nanofluids subject to Newtonian heating boundary condition. This approach efficiently refines the mesh in regions with steep velocity and thermal gradients, providing a stable and accurate framework for capturing complex viscoelastic flows.
- Numerical experiments demonstrate that the adaptive grid achieves 77.6–88.4% higher accuracy with enhanced convergence stability compared to uniform grids at the same grid scale. Grid points gradually cluster within the boundary layers, effectively capturing sharp gradients and thereby highlighting both computational efficiency and physical reliability.
- Parametric analysis reveals that the fractional derivative order α and the fractional integral index β have opposing influences on the velocity profile. Specifically, raising α or lowering β leads to a thicker velocity boundary layer, with the effect of β being more pronounced. These results highlight how the fractional model captures memory-dependent viscoelastic behavior.
- A comparison is conducted among four constitutive models: the classical Newtonian model, the ordinary Maxwell model, the single-parameter fractional Maxwell model, and the dual-fractional parameter Maxwell model. The results reveal that the dual-fractional Maxwell model exhibits the thickest momentum boundary layer, reflecting the enhanced historical dependence and memory effects, whereas the single-parameter fractional Maxwell model lies between the classical Newtonian and ordinary Maxwell models. Moreover, the fractional Cattaneo model produces a thinner thermal boundary layer than the ordinary Cattaneo model, highlighting the influence of fractional heat conduction on thermal transport.

This study provides an efficient numerical framework for simulating the transient, free convective flow of viscoelastic nanofluids under Newtonian heating, which is relevant to many heat transfer processes in engineering applications. The novelty of this work lies in combining fractional viscoelastic governing equations with an adaptive moving mesh scheme, which not only improves the resolution of sharp boundary layer gradients but also captures the intrinsic memory and nonlocal effects of fractional models. However, the present study is restricted to the vertical plate configuration and mainly focuses on the numerical implementation of the proposed scheme. A complete theoretical analysis of stability and error estimates is not provided here; it will instead be investigated in future work.

The structure of this work is as follows. Section 2 derives the fractional integrodifferential governing equations using a dual-parameter fractional Maxwell model and the generalized Cattaneo constitutive equation. The discretization scheme is established by using the finite difference method in Section 3. In Section 4, the adaptive grid is constructed based on the equidistribution principle of a monitor function.

Numerical simulations and validation of the adaptive algorithm are presented in Section 5. Finally, the main conclusions are summarized in Section 6.

2. Mathematical formulation

This study examines the natural convection flow and heat transfer of an incompressible nanofluid past an infinite vertical plate subjected to Newtonian heating and thermal radiative flux q_r. Figure 1 provides a schematic of the physical configuration: the x-axis is oriented vertically upward along the plate, and the y-axis is perpendicular to it. Because the plate extends infinitely in the x-direction, all physical quantities governing the fluid flow depend solely on y and t. Initially, the plate and the fluid remain stationary, maintaining a constant ambient temperature T_a. For $t > 0$, the local surface temperature T varies linearly with the heat transport from the plate to the fluid in accordance with the Newtonian heating condition. The fluid velocity is expressed as $U = u(y,t)e_x$. The fluid is a CuO-water nanofluid, and the corresponding thermophysical properties are summarized in Table 1. The assumptions made to idealize the proposed model are as follows:

(i) Nanoparticles and the base fluid are in local thermodynamic equilibrium;

(ii) Nanoparticles are uniformly sized and identical in shape;

(iii) The thermophysical properties of the nanofluid remain constant, except for variations influenced by the nanoparticle volume fraction;

(iv) The plate is impermeable, and viscous dissipation effects are neglected.

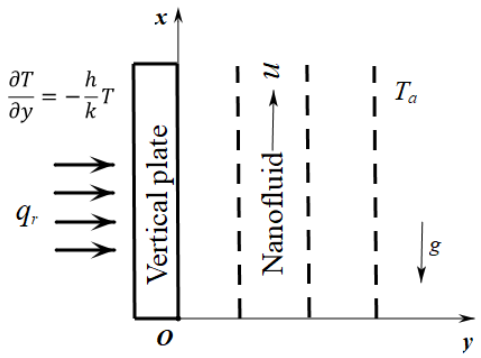

Figure 1. Schematic representation of the physical model.

Given the aforementioned assumptions, the governing boundary-layer equations describing the laminar hydromagnetic free convection flow of nanofluids are expressed as

$$\rho_{\mathrm{nf}} \frac{\partial u(y,t)}{\partial t} = \frac{\partial \sigma_{xy}}{\partial y} + (\rho\beta_T)_{\mathrm{nf}} g[T(y,t) - T_{\mathrm{a}}], \tag{2.1}$$

$$(\rho C_p)_{\mathrm{nf}} \frac{\partial T(y,t)}{\partial t} = -\frac{\partial q(y,t)}{\partial y}, \tag{2.2}$$

where ρ_{nf} denotes nanofluid density, σ_{xy} represents shear stress, $(\beta_T)_{\mathrm{nf}}$ is the volumetric coefficient of thermal expansion, g denotes the gravitational acceleration, $(C_p)_{\mathrm{nf}}$ represents specific heat capacity, and q is heat flux, respectively. In numerous engineering applications, Newtonian heating is widely adopted

in the design of heat exchange systems, where surrounding surfaces absorb thermal energy from solar irradiation or other sources. Most existing investigations on nanofluid flows have commonly imposed either prescribed wall temperature or specified heat flux as thermal boundary conditions. In this work, a Newtonian heating boundary condition is employed to characterize the convective heat transfer between the wall and the fluid. This thermal interaction is characterized by the heat transfer coefficient h and the thermal conductivity k. Far from the wall, the velocity and temperature are assumed to approach their ambient values, indicating an undisturbed quiescent fluid. Thus, the initial and boundary conditions are specified as

$$u(y,0)=0, \quad T(y,0)=T_a, \tag{2.3}$$

$$u(0,t)=0, \quad \left.\frac{\partial T(y,t)}{\partial y}\right|_{y=0}=-\frac{h}{k}T(0,t), \tag{2.4}$$

$$\lim_{y\to+\infty} u(y,t)=0, \quad \lim_{y\to+\infty} T(y,t)=T_a. \tag{2.5}$$

This study focuses on nanofluids containing spherical nanoparticles, for which the thermophysical properties are expressed in terms of their constituents [32]:

$$\mu_{\mathrm{nf}}=\frac{\mu_{\mathrm{f}}}{(1-\varphi)^{2.5}}, \quad \rho_{\mathrm{nf}}=(1-\varphi)\rho_{\mathrm{f}}+\varphi\rho_{\mathrm{s}}, \quad k_{\mathrm{nf}}=k_{\mathrm{f}}\left[\frac{k_{\mathrm{s}}+2k_{\mathrm{f}}-2\varphi(k_{\mathrm{f}}-k_{\mathrm{s}})}{k_{\mathrm{s}}+2k_{\mathrm{f}}+\varphi(k_{\mathrm{f}}-k_{\mathrm{s}})}\right],$$
$$\left(\rho C_p\right)_{\mathrm{nf}}=(1-\varphi)\left(\rho C_p\right)_{\mathrm{f}}+\varphi\left(\rho C_p\right)_{\mathrm{s}}, \quad (\rho\beta_T)_{\mathrm{nf}}=(1-\varphi)(\rho\beta_T)_{\mathrm{f}}+\varphi(\rho\beta_T)_{\mathrm{s}}.$$

Here, φ represents the nanoparticle volume fraction, and the subscripts "nf", "f", and "s" correspond to the nanofluid, base fluid, and nanoparticle, respectively. Based on the aforementioned assumptions, the governing fractional nanofluid equations incorporating Newtonian heating and thermal radiation are developed below.

Table 1. Thermophysical properties of the base fluid and nanoparticles.

Base fluid/ Nanoparticles	$\rho\left(kg/m^3\right)$	$C_p\,(J/kg/K)$	$k\,(W/m/K)$	$\beta_T\times10^5\,(1/K)$	$\mu\times10^3\,(kg/m/s)$
Water	997.1	4179	0.613	21	1.0019
CuO	6320	531.8	76.5	1.8	-

2.1. Preliminary knowledge

We first recall the definition of fractional calculus, which plays a fundamental role in modeling the viscoelastic behavior of nanofluids. The Caputo fractional derivative is adopted because it aligns naturally with the initial conditions, which are expressed using integer-order derivatives.

Definition 1. *[33] For any function $f\in L^1(D)$, the left-sided Riemann-Liouville fractional integral of order $\alpha>0$ is defined as*

$$I_t^{\alpha}f(t)=\frac{1}{\Gamma(\alpha)}\int_0^t(t-\eta)^{\alpha-1}f(\eta)\,d\eta,$$

where $L^1(D)$ denotes the space of Lebesgue integrable functions on $D=(0,t)$, and $\Gamma(\cdot)$ is the gamma function.

Definition 2. *[33] For any function $f \in L^1(D)$ and $n-1 < \alpha < n$, $n \in \mathbb{N}$, the left-sided Caputo fractional derivative of order α is defined as*

$$D_t^{\alpha} f(t) = I_t^{n-\alpha} f^{(n)}(t) = \frac{1}{\Gamma(n-\alpha)} \int_0^t (t-\eta)^{n-\alpha-1} f^{(n)}(\eta)\, d\eta.$$

2.2. Momentum equation

The classical single-parameter fractional Maxwell model can be derived from a mechanical analog consisting of a dashpot connected in series with a fractional viscoelastic element. The dashpot follows the constitutive relation $\sigma_1 = \mu D_t \varepsilon_1$, and the fractional element satisfies $\sigma_2 = E_2 \lambda_2^{\alpha_2} D_t^{\alpha_2} \varepsilon_2$, $0 < \alpha_2 < 1$ [34]. Here, σ_1 and σ_2 denote the stresses, ε_1 and ε_2 are the corresponding strains, μ is the viscosity, and E_2 and λ_2 represent the shear modulus and relaxation time of the fractional element. By enforcing stress equivalence ($\sigma = \sigma_1 = \sigma_2$) and strain additivity ($\varepsilon = \varepsilon_1 + \varepsilon_2$), the single-parameter fractional Maxwell constitutive relationship is obtained. However, this model has limitations in capturing complex rheological behaviors, particularly when multiple relaxation mechanisms are involved. To better describe the memory-dependent and nonlocal characteristics of viscoelastic nanofluids, we use a dual-parameter fractional Maxwell model, where both elements are replaced with fractional elements:

$$\sigma_1(t) = E_1 \lambda_1^{\alpha_1} D_t^{\alpha_1} \varepsilon_1(t), \quad 0 < \alpha_1 < 1, \tag{2.6}$$

$$\sigma_2(t) = E_2 \lambda_2^{\alpha_2} D_t^{\alpha_2} \varepsilon_2(t), \quad 0 < \alpha_2 < 1. \tag{2.7}$$

This leads to the dual-parameter fractional Maxwell model

$$\sigma(t) + \lambda^{\alpha_1-\alpha_2} D_t^{\alpha_1-\alpha_2} \sigma(t) = E \lambda^{\alpha_1} D_t^{\alpha_1} \varepsilon(t), \quad 0 < \alpha_1, \alpha_2 < 1, \tag{2.8}$$

where $\lambda = \left(E_1 \lambda_1^{\alpha_1} / E_2 \lambda_2^{\alpha_2}\right)^{1/(\alpha_1-\alpha_2)}$ and $E = E_1(\lambda_1/\lambda)^{\alpha_1}$. Without loss of generality, taking $\alpha = \alpha_1 - \alpha_2$, $\beta = \alpha_1$, Eq (2.8) can be rewritten as [35]

$$\sigma(t) + \lambda^{\alpha} D_t^{\alpha} \sigma(t) = E \lambda^{\beta} D_t^{\beta} \varepsilon(t), \quad 0 \le \alpha \le \beta \le 1. \tag{2.9}$$

From the perspective of mechanical construction, the dual-parameter fractional Maxwell model inherently implies the condition $\alpha \le \beta$, thereby avoiding the unphysical phenomenon of an increasing relaxation function [36] when $\alpha > \beta$. Compared with the single-parameter fractional Maxwell model, the dual-parameter fractional Maxwell model introduces two fractional orders that provide greater flexibility in characterizing viscoelastic memory effects. For $\alpha = \beta = 1$, the model (2.9) reduces to the classical Maxwell model, whereas for $\alpha = 0$ and $\beta = 1$, it recovers the classical Newtonian viscosity law. The derivative on the right-hand side of Eq (2.9) is represented by a fractional integral form [37], yielding the constitutive relation for nanofluids:

$$\sigma_{xy} + \lambda^{\alpha} D_t^{\alpha} \sigma_{xy} = \mu \lambda^{\beta-1} I_t^{1-\beta} \left(\frac{\partial u}{\partial y}\right). \tag{2.10}$$

By combining Eqs (2.1) and (2.10), the fractional integrodifferential momentum equation is formulated as

$$\left(1 + \lambda^{\alpha} D_t^{\alpha}\right) \frac{\partial u(y,t)}{\partial t} = \nu_{\mathrm{nf}} \lambda^{\beta-1} I_t^{1-\beta} \left(\frac{\partial^2 u(y,t)}{\partial y^2}\right) + g\,(\beta_T)_{\mathrm{nf}} \left(1 + \lambda^{\alpha} D_t^{\alpha}\right) [T(y,t) - T_a], \tag{2.11}$$

where $\nu_{\mathrm{nf}} = (\mu/\rho)_{\mathrm{nf}}$ represents the kinematic viscosity of the nanofluid.

2.3. Energy equation

Based on the Rosseland approximation, the radiation heat flux can be written as

$$q_r = -\frac{4\sigma_{SB}}{3k_R}\frac{\partial T^4}{\partial y}, \tag{2.12}$$

where σ_{SB} is the Stefan–Boltzmann constant, and k_R denotes the absorption coefficient. By applying a first-order Taylor expansion to T^4 about T_a, the net radiation heat flux absorbed by the nanofluid can be approximated as

$$q_r = -\frac{16\sigma_{SB}T_a^3}{3k_R}\frac{\partial T}{\partial y}. \tag{2.13}$$

Combining this with Fourier's law of heat conduction $q_c = -k\nabla T$, the effective conduction–radiation heat flux q_{eff} is expressed as

$$q_{\text{eff}} = q_c + q_r = -\left(k + \frac{16\sigma_{SB}T_a^3}{3k_R}\right)\frac{\partial T}{\partial y} \equiv -k_{\text{eff}}\frac{\partial T}{\partial y}, \tag{2.14}$$

where the effective thermal conductivity k_{eff} is defined by

$$k_{\text{eff}} = k + \frac{16\sigma_{SB}T_a^3}{3k_R}. \tag{2.15}$$

In the extension of Buongiorno's approach [38], the generalized Cattaneo constitutive relation incorporates a memory-dependent fractional-order derivative to capture the anomalous thermodynamic behavior of viscoelastic fluids, which accounts for the nonlocal heat flux history and finite propagation speed of thermal waves. Accordingly, we develop the energy equation for nanofluids using the generalized Cattaneo constitutive relation, incorporating the effective conduction–radiation heat flux [39]:

$$q_{\text{eff}} + \tau^\gamma D_t^\gamma q_{\text{eff}} = -k_{\text{eff}}\frac{\partial T}{\partial y}, \quad 0 \le \gamma \le 1, \tag{2.16}$$

where τ represents the temperature relaxation time. For $\gamma = 0$, the model (2.16) recovers the classical Fourier law, accounting for both conduction and radiation; for $\gamma = 1$, it reverts to the ordinary Cattaneo model with an effective heat flux combining conduction and radiation effects. Substituting Eq (2.16) into Eq (2.2) yields the following governing energy equation:

$$\left(1 + \tau^\gamma D_t^\gamma\right)\frac{\partial T(y,t)}{\partial t} = \frac{k_{\text{eff}}}{\left(\rho C_p\right)_{\text{nf}}}\frac{\partial^2 T(y,t)}{\partial y^2}. \tag{2.17}$$

2.4. Nondimensionalization

To maintain dimensional consistency, the following dimensionless variables are introduced:

$$y^* = \frac{Gr^{1/4}}{L}y, \quad t^* = \frac{\nu_{\text{nf}}Gr^{1/2}}{L^2}t, \quad u^* = \frac{L}{\nu_{\text{nf}}Gr^{1/2}}u, \quad T^* = \frac{T - T_{\text{a}}}{T_{\text{a}}},$$

$$\lambda^* = \frac{\nu_{\mathrm{nf}} Gr^{1/2}}{L^2}\lambda, \quad \tau^* = \frac{\nu_{\mathrm{nf}} Gr^{1/2}}{L^2}\tau, \quad Gr = \frac{gL^3 (\beta)_{\mathrm{nf}} T_{\mathrm{a}}}{\nu_{\mathrm{nf}}^2},$$

$$Pr = \frac{\mu_{\mathrm{nf}} \left(C_p\right)_{\mathrm{nf}}}{k_{\mathrm{nf}}}, \quad Nr = \frac{16\sigma_{_{SB}} T_{\mathrm{a}}^3}{3k_{\mathrm{nf}} k_{_R}}, \quad Pr_{\mathrm{eff}} = \frac{Pr}{1 + Nr},$$

where Gr represents the thermal Grashof number, Pr denotes the Prandtl number, and Nr is the thermal radiation parameter. The characteristic length is taken as $L = k/h$, which arises naturally from the Newtonian heating boundary condition and represents a thermal length scale associated with the balance between conductive and convective heat transfer. This choice simplifies the dimensionless boundary condition and does not affect the physical boundary layer thickness.

Substituting the nondimensional variables into the model and omitting the superscript "*", we obtain

$$(1 + \lambda^\alpha D_t^\alpha)\frac{\partial u}{\partial t} = \frac{1}{\lambda^{1-\beta}} I_t^{1-\beta}\left(\frac{\partial^2 u}{\partial y^2}\right) + (1 + \lambda^\alpha D_t^\alpha)T, \tag{2.18}$$

$$\left(1 + \tau^\gamma D_t^\gamma\right)\frac{\partial T}{\partial t} = \frac{1}{Pr_{\mathrm{eff}}}\frac{\partial^2 T\,(y,t)}{\partial y^2} \tag{2.19}$$

along with the nondimensional initial and boundary conditions

$$u\,(y,0) = 0, \quad T\,(y,0) = 0, \tag{2.20}$$

$$u\,(0,t) = 0, \quad \left.\frac{\partial T\,(y,t)}{\partial y}\right|_{y=0} = -Gr^{-1/4}\left[1 + T\,(0,t)\right], \tag{2.21}$$

$$\lim_{y\to+\infty} u\,(y,t) = 0, \quad \lim_{y\to+\infty} T\,(y,t) = 0. \tag{2.22}$$

Because the plate and the nanofluid are initially at rest and maintained at the ambient temperature, the initial acceleration and thermal rate are assumed to vanish, that is, $\partial u/\partial t\,(y,0) = 0$ and $\partial T/\partial t\,(y,0) = 0$. Together with initial conditions (2.20), the term $D_t^\alpha(\partial u/\partial t)$ is equivalent to $D_t^{\alpha+1}u$, ensuring that the systems (2.18)–(2.22) is well posed and admits a unique solution.

3. The discretization scheme

To construct our numerical scheme, we first consider an arbitrary nonuniform grid

$$\Omega^M = \{y_i \mid 0 = y_0 < y_1 < \cdots < y_{M-1} < y_M = L\},$$

where M is a positive discretization parameter. The spatial steps are given by $h_i = y_i - y_{i-1}$ $(1 \le i \le M)$. For the temporal domain, we define the mesh points as $t_n = n\Delta t$ $(n = 0, 1, \ldots, N)$, where $\Delta t = t_{\mathrm{total}}/N$ denotes the uniform temporal step size. For any grid function $u_i^n = u(y_i, t_n)$ and $T_i^n = T(y_i, t_n)$, we introduce the following notations:

$$D^- u_i^n = \frac{u_i^n - u_{i-1}^n}{h_i}, \quad D^+ u_i^n = \frac{u_{i+1}^n - u_i^n}{h_{i+1}}, \quad \hbar = \frac{h_i + h_{i+1}}{2},$$

$$Du_i^n = \frac{u_{i+1}^n - u_i^n}{\hbar}, \quad \nabla_t u_i^n = \frac{u_i^n - u_i^{n-1}}{\Delta t}.$$

We discretize the governing Eqs (2.18) and (2.19) at the grid point (y_i, t_n). The integer-order derivatives are approximated as follows:

$$\frac{\partial \mathrm{u}\,(y_i,t_n)}{\partial t} = \nabla_t u_i^n + O\,(\Delta t)\,, \quad \frac{\partial T\,(y_i,t_n)}{\partial t} = \nabla_t T_i^n + O\,(\Delta t)\,, \quad \frac{\partial^2 T\,(y_i,t_n)}{\partial y^2} = DD^- T_i^n + O\left((\Delta y)^2\right).$$

The Caputo time-fractional derivatives are approximated by the L1 algorithm for orders $\alpha \in (0,1)$ and $\alpha + 1 \in (1,2)$, as described in [12]. For the coupled temporal fractional-order integral and spatial derivative in the convective term $I_t^{1-\beta}(\partial^2 u(y,t)/\partial y^2)$, we employ the weighted-shifted Grünwald difference scheme [40]

$$\begin{aligned} I_t^{1-\beta}\left(\frac{\partial^2 u(y_i,t_n)}{\partial y^2}\right) &= (\Delta t)^{1-\beta}\left[\frac{1+\beta}{2}\sum_{k=0}^{n}\omega_k^{(1-\beta)} DD^- u_i^{n-k} + \frac{1-\beta}{2}\sum_{k=0}^{n-1}\omega_k^{(1-\beta)} DD^- u_i^{n-k-1}\right] \\ &= (\Delta t)^{1-\beta}\sum_{k=0}^{n}\gamma_k^{(\beta)} DD^- u_i^{n-k} + O\left((\Delta t)^2 + (\Delta y)^2\right), \end{aligned} \tag{3.1}$$

where $\omega_k^{(1-\beta)} = (-1)^k\binom{\beta-1}{k}$, $\gamma_0^{(\beta)} = (1+\beta)\omega_0^{(1-\beta)}/2$, $\gamma_k^{(\beta)} = (1+\beta)\omega_k^{(1-\beta)}/2 + (1-\beta)\omega_{k-1}^{(1-\beta)}/2$, $k \geq 1$.

Using the above approximations, we obtain the upwind finite difference scheme of the governing equations

$$\begin{aligned} &\nabla_t u_i^n + \frac{\lambda^\alpha (\Delta t)^{-\alpha}}{\Gamma(2-\alpha)}\left[a_0^{(\alpha)}\nabla_t u_i^n - \sum_{k=1}^{n-1}\left(a_{n-k-1}^{(\alpha)} - a_{n-k}^{(\alpha)}\right)\nabla_t u_i^k - a_{n-1}^{(\alpha)}\nabla_t u_i^0\right] \\ &= \lambda^{\beta-1}(\Delta t)^{1-\beta}\sum_{k=0}^{n}\gamma_k^{(\beta)} DD^- u_i^{n-k} + T_i^n + \frac{\lambda^\alpha (\Delta t)^{1-\alpha}}{\Gamma(2-\alpha)}\sum_{k=1}^{n} a_{n-k}^{(\alpha)}\nabla_t T_i^k, \end{aligned} \tag{3.2}$$

$$\nabla_t T_i^n + \frac{\tau^\gamma (\Delta t)^{-\gamma}}{\Gamma(2-\gamma)}\left[a_0^{(\gamma)}\nabla_t T_i^n - \sum_{k=1}^{n-1}\left(a_{n-k-1}^{(\gamma)} - a_{n-k}^{(\gamma)}\right)\nabla_t T_i^k - a_{n-1}^{(\gamma)}\nabla_t T_i^0\right] = \frac{1}{Pr_{\mathrm{eff}}} DD^- T_i^n, \tag{3.3}$$

where $u_i^{-1} = u_i^0 - \Delta t\,\partial u(y_i,0)/\partial t$, $T_i^{-1} = T_i^0 - \Delta t\,\partial T(y_i,0)/\partial t$, and $a_k^{(\zeta)} = (k+1)^{1-\zeta} - k^{1-\zeta}$, $\zeta = \alpha, \gamma$, $k = 0, 1, 2, ..., n-1$, and the truncation errors of the scheme are of order $O\left(\Delta t + (\Delta y)^2\right)$.

The discretization of the dimensionless initial and boundary conditions is presented as

$$u_i^0 = 0,\ T_i^0 = 0, \quad 0 \leq i \leq M; \tag{3.4}$$

$$u_0^n = 0,\ D^+ T_0^n = -Gr^{-1/4}\left[1 + T_0^n\right],\ u_M^n = 0,\ T_M^n = 0, \quad 1 \leq n \leq N. \tag{3.5}$$

Remark 1. The L1 algorithm and the weighted-shifted Grünwald difference scheme are usually derived under certain regularity assumptions on the exact solution. However, solutions of time-fractional differential equations often exhibit weak singularities near the initial time $t = 0$, which may deteriorate the accuracy of numerical schemes on uniform time meshes. To address this issue, nonuniform time discretization strategies, such as graded meshes or adaptive meshes, can be employed [41–43]. The development and rigorous analysis of such techniques are beyond the scope of the present paper.

4. Adaptive grid algorithm

Adaptive moving grids have been widely employed in singular perturbation problems [44–47] due to their capability to accurately resolve boundary layer structures and regions with sharp gradients. To capture the steep gradients in the nanofluid velocity and thermal boundary layers effectively, an adaptive grid method is implemented in the spatial domain. The adaptive grid Ω^M is constructed through the equidistribution of a positive monitor function $M(y)$ satisfying

$$\int_{y_{i-1}}^{y_i} M(y)dy = \int_{y_i}^{y_{i+1}} M(y)dy, \quad i = 1, \cdots, M-1. \tag{4.1}$$

Equivalently, Eq (4.1) can be expressed as

$$\int_{y_{i-1}}^{y_i} M(y)dy = \frac{1}{M}\int_0^L M(y)dy, \quad i = 1, \cdots, M. \tag{4.2}$$

For a quasilinear, one-dimensional convection–diffusion equation solved by the upwind finite difference method, the arc-length function $M(y) = \sqrt{1 + (\phi'(y))^2}$ is widely adopted, where $\phi(y)$ is the exact solution of the problem [48]. Motivated by the work of Liu et al. [30] on an adaptive moving grid for coupled convection-diffusion equations, the following monitor function is employed in practical computations:

$$\tilde{M}(y) \triangleq \tilde{M}(y, t_n) = \sqrt{1 + \max_{y\in[0,L]}\left[\left(\frac{\partial u(y,t_n)}{\partial y}\right)^2, \left(\frac{\partial T(y,t_n)}{\partial y}\right)^2\right]}, \tag{4.3}$$

where $u(y, t_n)$ and $T(y, t_n)$ represent velocity and temperature solutions at time t_n. The discrete counterpart is given by

$$\tilde{M}_i = \tilde{M}(y_i, t_n) = \sqrt{1 + \max\left[\left(D^- u_i^n\right)^2, \left(D^- T_i^n\right)^2\right]}. \tag{4.4}$$

To construct this adaptive grid and obtain the associated numerical solution, the following iterative algorithm is employed:

Step 1: The initial grid is taken as a uniform grid $\Omega^{M,(0)} = \left\{y_i^{(0)} \middle| y_i^{(0)} = i/M, 0 \le i \le M\right\}$. Set termination threshold $\gamma^* > 1$.

Step 2: For iteration k, solve governing equations (3.2)–(3.5) on current grid $\Omega^{M,(k)} = \left\{y_i^{(k)} \middle| 0 \le i \le M\right\}$ to obtain solutions $\left\{u_i^{M,(k)}\right\}_{i=0}^M$ and $\left\{T_i^{M,(k)}\right\}_{i=0}^M$. Define the grid step sizes as $h_i^{(k)} = y_i^{(k)} - y_{i-1}^{(k)}$ and compute $\tilde{M}_i^{(k)}$.

Step 3: Set $L_0^{(k)} = 0$ and $L_i^{(k)} = \sum_{j=1}^{i} h_j^{(k)} \tilde{M}_j^{(k)}$ for $i = 1, 2, \cdots, M$. If the stopping criterion

$$\frac{\max_{1\le i\le M} h_i^{(k)} \tilde{M}_i^{(k)}}{L_M^{(k)}} \le \frac{\gamma^*}{M}$$

holds true, continue to Step 5.

Step 4: Construct interpolation nodes $Y_i^{(k)} = iL_M^{(k)}/M$ for $i = 0, 1, \cdots, M$. $\left(Y_i^{(k)}, y_i^{(k+1)}\right)$ is interpolated linearly to $\left(L_i^{(k)}, y_i^{(k)}\right)$, which leads to the generation of a new grid $\Omega^{M,(k+1)} = \left\{y_i^{(k+1)} \middle| 0 \le i \le M\right\}$. Let $k = k + 1$ and return to Step 2.

Step 5: Store the final grid and solutions

$$\Omega^{M,*} = \Omega^{M,(k)}, \quad \left\{u_i^{M,*}\right\}_{i=0}^{M} = \left\{u_i^{M,(k)}\right\}_{i=0}^{M}, \quad \left\{T_i^{M,*}\right\}_{i=0}^{M} = \left\{T_i^{M,(k)}\right\}_{i=0}^{M},$$

then terminate the iteration process.

Furthermore, to enhance the reproducibility of the adaptive grid implementation, we give the following pseudocode:

Algorithm: Adaptive moving grid algorithm

Input: Initial uniform grid $y^1 \in \mathbb{R}^{M+1}$, time steps N, spatial intervals M, threshold γ^*
Output: $\boldsymbol{\Omega} \in \mathbb{R}^{(M+1)\times(N+1)}$, $\boldsymbol{U} \in \mathbb{R}^{(M+1)\times(N+1)}$, $\boldsymbol{T} \in \mathbb{R}^{(M+1)\times(N+1)}$

// Step 1: Initialization
$y_i^{(1)} \leftarrow i \cdot y_{\max}/M, \quad i = 0, 1, \ldots, M$
$\boldsymbol{\Omega}(:, 1) \leftarrow y^{(1)}$
$\gamma^* \leftarrow 1.1$

for $k = 2$ to $N + 1$ **do**
    converged $\leftarrow$ false
    $\boldsymbol{y}^{(k)} \leftarrow \boldsymbol{\Omega}(:, k-1)$
    while not converged **do**
// Step 2.1: Compute grid spacing
        for $i = 1$ to M **do**
            $h_i \leftarrow y_{i+1}^{(k)} - y_i^{(k)}$
        end for
// Step 2.2: Solve governing equations
        $[\boldsymbol{u}^{(k)}, \boldsymbol{T}^{(k)}] \leftarrow \text{SolveEquations}(\boldsymbol{U}, \boldsymbol{T}, \boldsymbol{y}^{(k)})$
// Step 3.1: Compute arc-length monitor function
        for $i = 1$ to M **do**
            $l_i^{(u)} \leftarrow \sqrt{h_i^2 + (u_{i+1}^{(k)} - u_i^{(k)})^2}$
            $l_i^{(T)} \leftarrow \sqrt{h_i^2 + (T_{i+1}^{(k)} - T_i^{(k)})^2}$
            $l_i \leftarrow \max\{l_i^{(u)}, l_i^{(T)}\}$
        end for
// Step 3.2: Compute cumulative arc-length
        $L_0 \leftarrow 0$
        for $i = 1$ to M **do**
            $L_i \leftarrow L_{i-1} + l_i$

end for
// Step 3.3: Compute mesh adaptation indicator
$\gamma_0 \leftarrow \dfrac{M}{L_M} \cdot \max\limits_{1\le i\le M}\{l_i\}$
if $\gamma_0 < \gamma^*$ **then**
// Step 5: Store the final grid and solutions
$\boldsymbol{\Omega}(:,k) \leftarrow \boldsymbol{y}^{(k)}$
$\boldsymbol{U}(:,k) \leftarrow \boldsymbol{u}^{(k)}$
$\boldsymbol{T}(:,k) \leftarrow \boldsymbol{T}^{(k)}$
converged $\leftarrow$ true
else
// Step 4.1: Construct interpolation nodes
for $j = 1$ to $M+1$ **do**
$Y_j \leftarrow (j-1)\cdot L_M/M$
end for
// Step 4.2: Linear interpolation to obtain new grid
for $j = 1$ to $M+1$ **do**
$y_j^{(k)} \leftarrow \text{Interpolate}(L \to y^{(k)}, Y_j)$
end for
end if
end while
end for
return $\boldsymbol{\Omega}, \boldsymbol{U}, \boldsymbol{T}$

5. Numerical results and discussion

Numerical experiments are conducted for the fractional nanofluid models (2.18)–(2.22), and the maximum errors and convergence orders of uniform and adaptive grids are compared. Next, the influences of fractional orders α, β, γ on the dimensionless velocity and temperature distributions are graphically displayed and analyzed in detail. Finally, we present a comparative analysis of different models to highlight the memory effect of fractional nanofluids. All numerical computations were implemented in MATLAB R2016a using a LENOVO laptop equipped with an AMD Ryzen 5 3500U CPU operating at 2.10 GHz and 8 GB RAM.

5.1. Error and convergence analysis

Because the analytical solution of the model is unavailable, the following formula is utilized to compute the error and convergence order:

$$e_n^M = \max_{i=0,1,\cdots,M} \left|\hat{u}_i^{2M} - u_i^M\right|, \quad p_n^M = \frac{\ln\left(e_n^M/e_n^{2M}\right)}{\ln 2},$$

where $\widehat{u}_i^{2M}$ represents the value corresponding to the original grid in the numerical solution obtained from the refined grid $\Omega^{2M} = \Omega^M \cup \{(y_i + y_{i+1})/2\}_{i=0}^{M-1}$ at t_n. The maximum pointwise error and convergence

order of the numerical solution are given by

$$e^M = \max_{n=0,1,\cdots,N} e_n^M, \quad p^M = \frac{\ln\left(e^M/e^{2M}\right)}{\ln 2}.$$

In the calculation, the parameters used in the model are set as follows: $\lambda = \tau = 0.2$, $\alpha = 0.2, \beta = 0.8$, $\gamma = 0.5$, $\varphi = 0.05$, $Gr = 6.4$, $Pr_{\text{eff}} = 5.8$, and $t_{\text{total}} = 30$. The termination threshold γ^* in the algorithm is 1.1. The performance of the adaptive grid method is evaluated through numerical experiments, with results summarized in Table 2, which lists the errors and convergence orders for both velocity and temperature. For fixed $\Delta t = 1/100$, the error decreases to approximately half as M doubles and the convergence order in the spatial direction reaches first order. The adaptive grid method maintains stable convergence across M, though a slight decline in order occurs at finer grids (e.g., M=1024).

Table 2. Maximum errors and convergence orders of $u(y,t)$ and $T(y,t)$ on the proposed adaptive grid.

	u		T	
M	Error	Order	Error	Order
64	3.0768×10^{-1}	1.057	6.4983×10^{-1}	1.072
128	1.4792×10^{-1}	0.996	3.0918×10^{-1}	1.011
256	7.4186×10^{-2}	1.050	1.5346×10^{-1}	1.039
512	3.5818×10^{-2}	0.994	7.4701×10^{-2}	0.997
1024	1.7989×10^{-2}	0.979	3.7419×10^{-2}	0.993
2048	9.1291×10^{-3}	–	1.8799×10^{-2}	–

Table 3. Maximum errors and convergence orders of $u(y,t)$ and $T(y,t)$ on the uniform grid.

	u		T	
M	Error	Order	Error	Order
64	2.6484	1.457	5.2531	1.532
128	9.6471×10^{-1}	1.206	1.8162	1.239
256	4.1819×10^{-1}	1.098	7.6947×10^{-1}	1.114
512	1.9534×10^{-1}	1.048	3.5556×10^{-1}	1.056
1024	9.4476×10^{-2}	1.024	1.7107×10^{-1}	1.027
2048	4.6469×10^{-2}	–	8.3920×10^{-2}	–

For comparison, the schemes (3.2)–(3.5) is also applied to the model on a uniform grid, defined as $\bar{\Omega}^M = \{y_i | y_i = i/M, 0 \le i \le M\}$. As shown in Tables 2 and 3, the adaptive grid method provides higher accuracy than the corresponding uniform mesh, with the error reduced by at least 77.6% ($T, M = 2048$), up to a maximum of 88.4% ($u, M = 64$). Figures 2 and 3 illustrate the pointwise error distributions of the velocity and temperature fields, with subfigures (a) and (b) representing adaptive and uniform grids, respectively. Overall, the adaptive grid yields lower errors within both velocity and thermal boundary layers compared to the uniform grid, with the most significant reduction observed near $y = 0$. As shown

in Figure 2, the adaptive grid captures sharp peaks and fine structures near boundaries, whereas the uniform grid produces smoother results. Similarly, the temperature field on the adaptive grid exhibits steeper thermal gradients and sharper localized features compared to the uniform grid, as demonstrated in Figure 3. Figure 4 displays the maximum pointwise errors of the fractional nanofluid model on logarithmic scales for both adaptive and uniform meshes. It can be seen that the adaptive grid reduces errors by approximately one order of magnitude compared to the uniform mesh. Although both meshes achieve roughly first-order convergence, the adaptive grid's orders are more consistent, whereas the uniform mesh exhibits greater fluctuation, particularly for sufficiently small M.

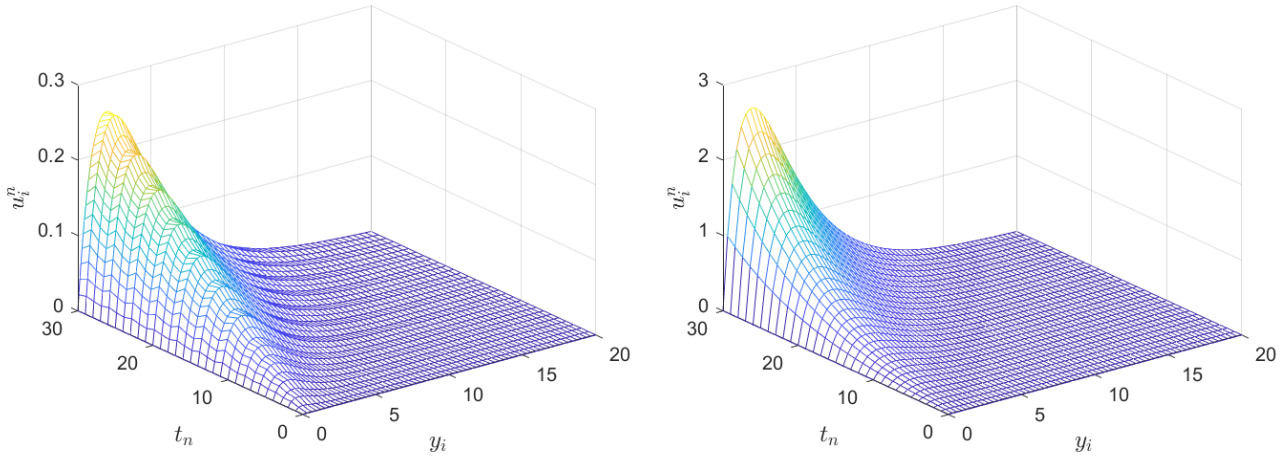

(a) Adaptive grid **(b)** Uniform grid

Figure 2. Pointwise error distribution of velocity field with $M = 64$ and $N = 30$.

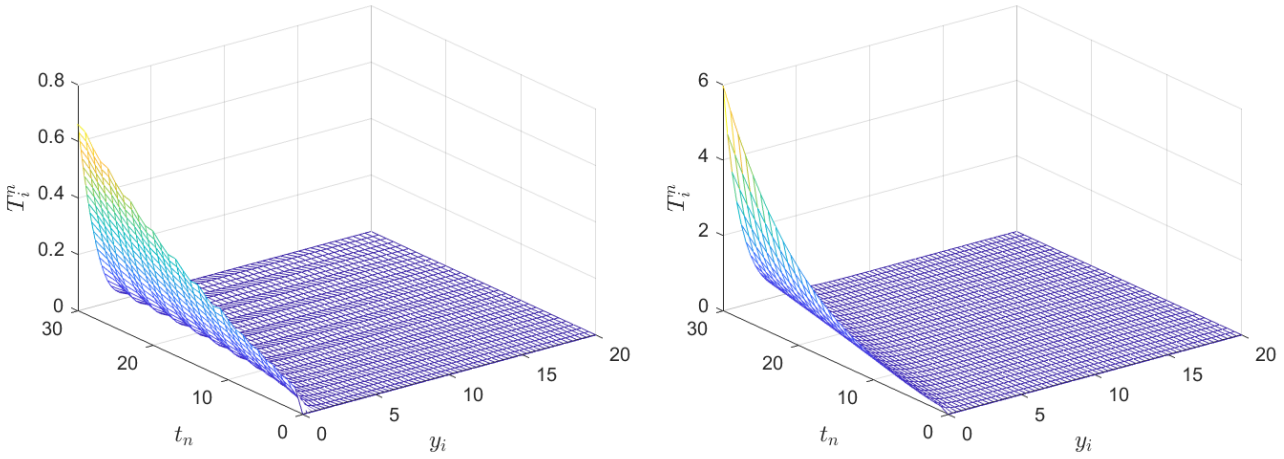

(a) Adaptive grid **(b)** Uniform grid

Figure 3. Pointwise error distribution of temperature field with $M = 64$ and $N = 30$.

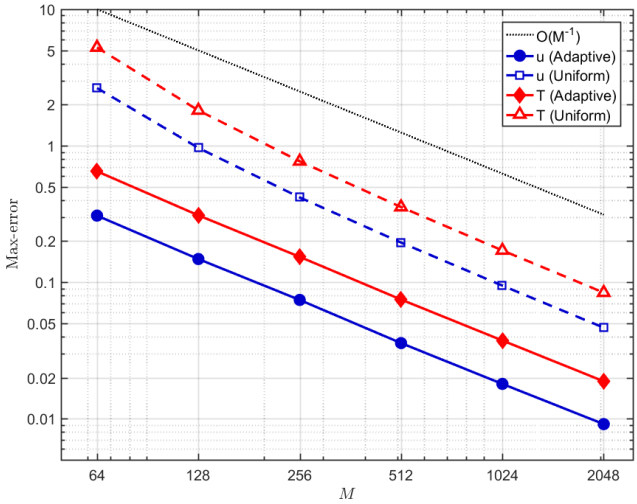

Figure 4. Maximum pointwise errors of log-log plot for fractional nanofluid model.

The behaviors of the numerical solutions on the adaptive grid are presented in Figure 5. Significant variations in both velocity and temperature solutions occur within the boundary layer near $y = 0$, subsequently asymptotically approaching zero. Figure 6 displays the grid movement process when solving the model using the adaptive grid algorithm. Over time, the grid nodes progressively concentrate toward the boundary layers, demonstrating the algorithm's capability to automatically refine the regions with drastic changes.

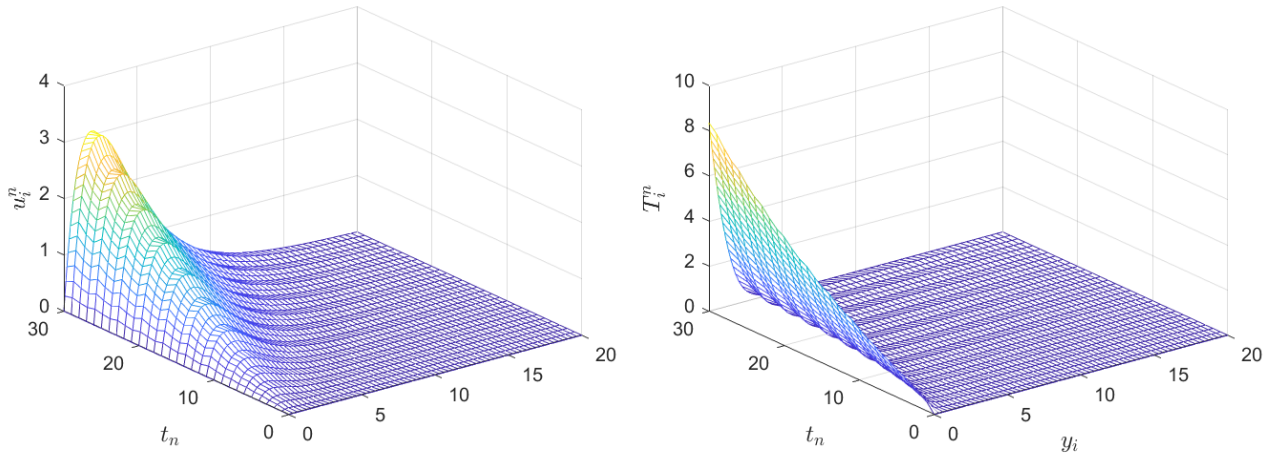

(a) Velocity distribution **(b)** Temperature distribution

Figure 5. Numerical solutions with $M = 64$ and $N = 30$.

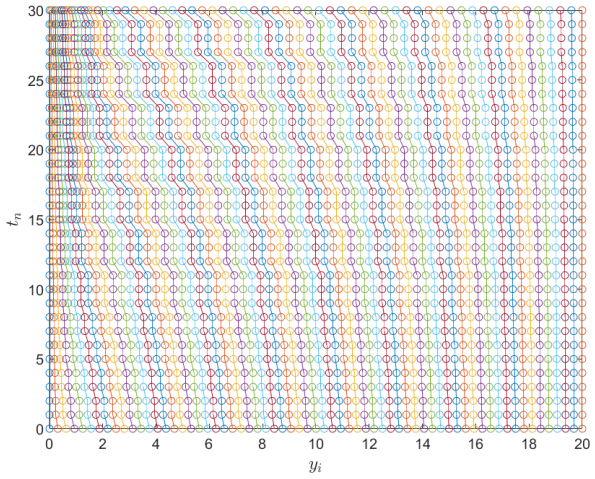

Figure 6. Evolution of the mesh with $M = 64$ and $N = 30$.

5.2. *Effects of fractional parameters on the velocity and temperature fields*

Figure 7 depicts the impact of the fractional derivative order α and integral index β on the velocity distribution. For different α values, the velocity of the nanofluid first rises and then slowly decays, reflecting the subdiffusive behavior of viscoelastic fluids. Higher values of α lead to a reduced maximum velocity, with the peak position further away from the plate. Notably, the velocity distributions with varying α values intersect at a specific point, beyond which the trend reverses; that is, a smaller α corresponds to a faster velocity decay. Consequently, the velocity boundary layer thickens as α increases. In contrast, the effect of β is entirely opposite and more pronounced (see Figure 7(b)). Specifically, a smaller β is associated with a lower peak velocity, whereas an increase in β results in the velocity increasing and decreasing more rapidly.

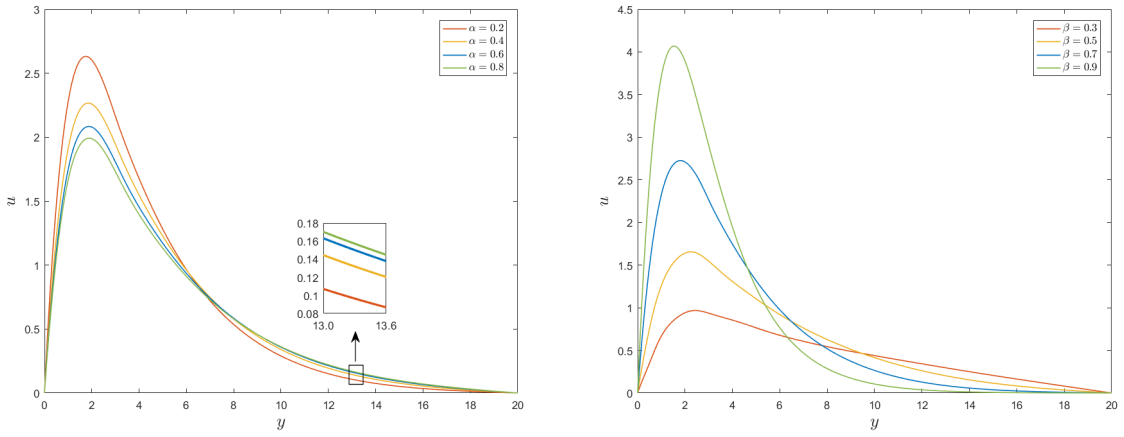

(a) Effects of α **(b)** Effects of β

Figure 7. Velocity distribution for the fractional derivative order α ($\beta = 0.8$) and the fractional integral index β ($\alpha = 0.1$) for fixed $\tau = 0.2$, $\gamma = 0.5$, $Pr_{\text{eff}} = 5.7$, and $Gr = 8.7$.

Figure 8 presents the variations in velocity and temperature fields due to the fractional derivative order γ. As depicted by Figure 8(a), the velocity profile exhibits increased peak values with higher γ, indicating enhanced acceleration in the nanofluid flow. An increase in γ gradually raises the temperature of the nanofluid, which is shown in Figure 8(b). It can be seen that increases in γ lead to thicker velocity and thermal boundary layers.

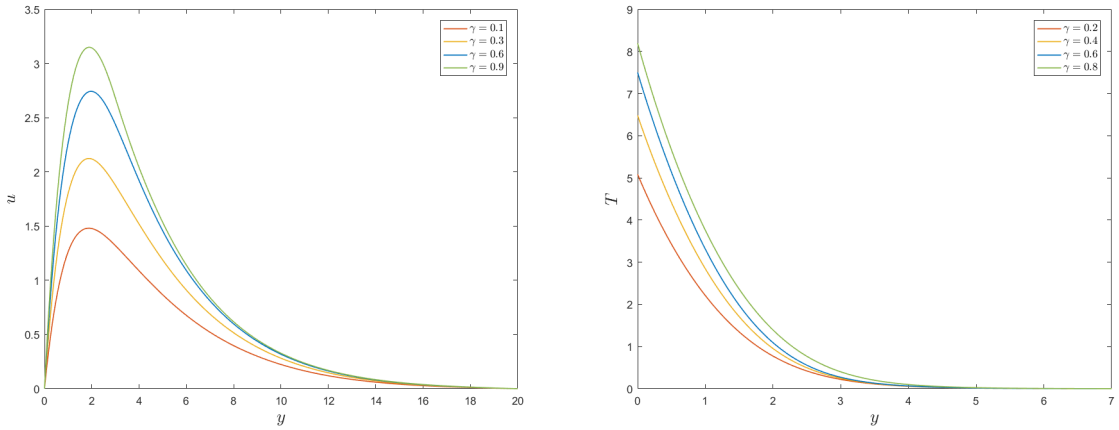

(a) Effects of γ on u **(b)** Effects of γ on T

Figure 8. Velocity and temperature distribution for the fractional derivative order γ, where (a) $\lambda = 0.2$, $\alpha = 0.2$, and $\beta = 0.8$; (b) $\tau = 0.2$ and $Pr_{\text{eff}} = 5.7$.

5.3. Comparison with different nanofluid models

As demonstrated in Section 2, setting $\alpha = 0.3, \beta = 1$ simplifies the constitutive relation (2.9) to the single-parameter fractional Maxwell model. Maintaining $\alpha = 0.3$ but adjusting $\beta = 0.7$ transforms it into the dual-fractional parameter Maxwell model. By incorporating fractional order terms into the ordinary Cattaneo model with the parameter $\gamma = 0.5$, the fractional Cattaneo law is established. Figure 9 compares different nanofluid models with respect to the velocity and temperature fields. In the classical Newtonian model, the nanofluid attains its maximum velocity and exhibits the sharpest acceleration/deceleration, as shown in Figure 9(a). For the single-parameter fractional Maxwell nanofluid model, the thickness of the velocity profile lies between that of the classical Newtonian model and the ordinary Maxwell model. It is evident that the velocity boundary layer thickness increases with an increase in the fractional parameter α. Furthermore, the velocity boundary layer is thickest in the dual-fractional parameter Maxwell nanofluid model, which effectively captures the historical dependence and memory effects of viscoelastic fluids. In terms of the temperature boundary layer thickness, Figure 9(b) presents a comparison between the proposed fractional Cattaneo nanofluid model and the ordinary Cattaneo nanofluid model. The fractional Cattaneo nanofluid model exhibits a thinner thermal boundary layer, highlighting the influence of fractional-order parameters on heat conduction mechanisms.

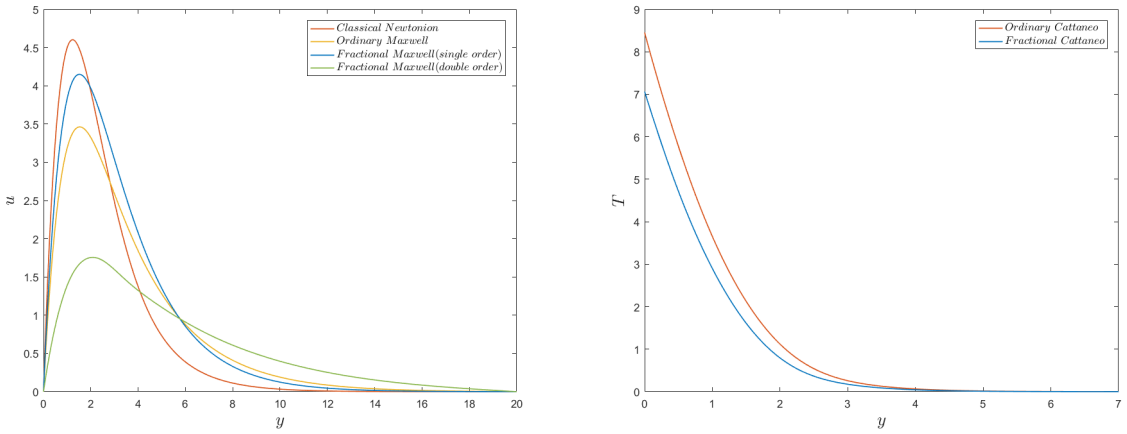

(a) Effects of different models on u **(b)** Effects of different models on T

Figure 9. Velocity and temperature distribution for the different models with $\lambda = \tau = 0.2$, $Pr_{\text{eff}} = 5.7$, and $Gr = 8.7$.

6. Conclusions

This work proposed an adaptive grid method to solve the fractional integrodifferential governing equations of viscoelastic nanofluid. To capture the complex rheological behavior of viscoelastic fluids, the dual-parameter fractional Maxwell model and the fractional Cattaneo model were employed, incorporating memory effects and nonlocal characteristics in the nonlinear fluid model. The governing equations were numerically solved using an upwind difference scheme combined with the L1 algorithm and the weighted-shifted Grünwald difference operator. A comprehensive parametric analysis was performed to evaluate the impact of fractional parameters on velocity and temperature fields. Additionally, a comparative study was performed between the proposed fractional constitutive model and other models. The main findings are summarized as follows:

(i) The adaptive grid method is superior to the uniform mesh in accuracy and stability for resolving coupled velocity-temperature nanofluid model, particularly for long-duration simulations. It can achieve higher accuracy with fewer grid points, whereas the uniform mesh requires significantly finer meshes to match the corresponding precision. This advantage stems from the method's ability to prioritize computation in regions of high gradient, a capability fundamentally lacking in uniform mesh.

(ii) The fractional derivative order α and the fractional integral index β exert opposing influences on the velocity profile. Increases in α or decreases in β lead to a thicker momentum boundary layer, with the impact of β being more pronounced. Both the momentum and thermal boundary layers thicken with increasing temperature fractional derivative γ, reflecting the memory and nonlocal effects captured by the fractional models.

(iii) Among the constitutive models, the velocity boundary layer progressively thickens from the classical Newtonian model to the ordinary Maxwell model, reaching a maximum in the dual-fractional Maxwell model due to enhanced historical dependence and memory effects. In contrast, the fractional Cattaneo model yields a thinner thermal boundary layer than the ordinary Cattaneo model, highlighting the influence of fractional heat conduction on thermal transport.

In this study, we focused on applying the proposed adaptive moving grid finite difference scheme to solve the fractional nanofluid model and evaluated its performance through numerical error and convergence analyses. Although a complete theoretical proof of stability and error is not provided, the scheme exhibits consistent and reliable behavior across different mesh resolutions. Future work could involve conducting rigorous stability and error analyses to further strengthen the theoretical foundation, as well as incorporating fast algorithms, such as the sum-of-exponentials (SOE) approximation [50] and parallel-in-time (PinT) methods [51], to improve computational efficiency for large-scale simulations. In addition, adaptive algorithms in the temporal direction will be investigated to further improve computational efficiency, and the model will be extended to incorporate nanoparticle transport mechanisms such as Brownian diffusion and thermophoretic effects [52, 53].

Nomenclature

C_p	Specific heat capacity
D_t^α	Caputo fractional derivative
E, E_1, E_2	Shear modulus
g	Gravitational acceleration
Gr	Grashof number
h	Heat transfer coefficient
I_t^α	Riemann–Liouville fractional integral
k	Thermal conductivity
k_R	Rosseland mean absorption coefficient
L	Characteristic length
Nr	Thermal radiation parameter
Pr	Prandtl number
q	Heat flux
q_c	Conduction heat flux
q_r	Radiative heat flux
T	Nanofluid temperature
T_a	Ambient temperature
u	Nanofluid velocity

Greek symbols

$\alpha, \alpha_1, \alpha_2$	Fractional order
β	Fractional order
β_T	Volumetric coefficient of thermal expansion
γ	Fractional order
γ^*	Termination threshold
$\varepsilon, \varepsilon_1, \varepsilon_2$	Shear strain
$\lambda, \lambda_1, \lambda_2$	Relaxation time
μ	Dynamic viscosity
ν	Kinematic viscosity
ρ	Density
$\sigma, \sigma_1, \sigma_2, \sigma_{xy}$	Shear stress
σ_{SB}	Stefan–Boltzmann constant
τ	Relaxation time
φ	Nanoparticle volume fraction

Subscripts

eff	Effective
f	Base fluid
nf	Nanofluid
s	Nanoparticle

Use of AI tools declaration

The authors declare they have not used Artificial Intelligence (AI) tools in the creation of this article.

Acknowledgments

This work was financially supported by the National Natural Science Foundation of China (Grant No. 12471391), the Science and Technology Foundation of Guizhou Province of China (Grant No. MS (2026) 798), the Natural Science Foundation of Anhui Provincial Universities (Grant No. 2024AH051364), the Australian Research Council via the Discovery Project (DP230102414), and the Research and Development Project of Henan Province (Science and Technology Cooperation Project, No. 252102521012).

Conflict of interest

The authors declare there is no conflict of interest.

Author contributions

Zhi Mao: Conceptualization, Methodology, Software, Validation, Writing – original draft, Funding acquisition. **Huafang Li:** Investigation, Software, Validation, Writing – original draft. **Xiaobing Bao:** Methodology, Software, Validation, Funding acquisition. **Leilei Wei:** Writing – review & editing, Funding acquisition. **Libin Liu:** Methodology, Writing – review & editing, Supervision. **Libo Feng:** Supervision, Writing – review & editing, Funding acquisition.

References

1. R. P. Chhabra, Non-Newtonian fluids: An introduction, in *Rheology of Complex Fluids* (eds. J. Krishnan, A. Deshpande, P. Kumar), Springer, New York, (2010), 3–34. https://doi.org/10.1007/978-1-4419-6494-6
2. J. Azaiez, G. M. Homsy, Linear stability of free shear flow of viscoelastic liquids, *J. Fluid Mech.*, **268** (1994), 37–69. https://doi.org/10.1017/S0022112094001254
3. D. Tripathi, S. K. Pandey, S. Das, Peristaltic flow of viscoelastic fluid with fractional Maxwell model through a channel, *Appl. Math. Comput.*, **215** (2010), 3645–3654. https://doi.org/10.1016/j.amc.2009.11.002
4. H. Qi, M. Xu, Some unsteady unidirectional flows of a generalized Oldroyd-B fluid with fractional derivative, *Appl. Math. Model.*, **33** (2009), 4184–4191. https://doi.org/10.1016/j.apm.2009.03.002
5. D. Song, T. Jiang, Study on the constitutive equation with fractional derivative for the viscoelastic fluids-modified Jeffreys model and its application, *Rheol. Acta*, **37** (1998), 512–517. https://doi.org/10.1007/s003970050138
6. F. Irgens, *Rheology and Non-Newtonian Fluids*, Springer, New York, 2014. https://doi.org/10.1007/978-3-319-01053-3
7. J. Zhao, L. Zheng, X. Zhang, F. Liu, Unsteady natural convection boundary layer heat transfer of fractional Maxwell viscoelastic fluid over a vertical plate, *Int. J. Heat Mass Transfer.*, **97** (2016), 760–766. https://doi.org/10.1016/j.ijheatmasstransfer.2016.02.059
8. L. Liu, L. Feng, Q. Xu, L. Zheng, F. Liu, Flow and heat transfer of generalized Maxwell fluid over a moving plate with distributed order time fractional constitutive models, *Int. Commun. Heat Mass Transfer.*, **116** (2020), 104679. https://doi.org/10.1016/j.icheatmasstransfer.2020.104679
9. L. Feng, F. Liu, I. Turner, V. V. Anh, Magnetohydrodynamics flow and heat transfer of novel generalized Kelvin–Voigt viscoelastic nanofluids over a moving plate, *Phys. Fluids*, **36** (2024), 063109. https://doi.org/10.1063/5.0213855
10. D. Qaiser, Z. Zheng, M. R. Khan, Numerical assessment of mixed convection flow of Walters-B nanofluid over a stretching surface with Newtonian heating and mass transfer, *Therm. Sci. Eng. Prog.*, **22** (2021), 100801. https://doi.org/10.1016/j.tsep.2020.100801

11. M. Aleem, M. I. Asjad, A. Shaheen, I. Khan, MHD Influence on different water based nanofluids (TiO_2, Al_2O_3, CuO) in porous medium with chemical reaction and newtonian heating, *Chaos Solitons Fractals*, **130** (2020), 109437. https://doi.org/10.1016/j.chaos.2019.109437

12. Z. Mao, L. Feng, I. Turner, A. Xiao, F. Liu, Transient free convective flow of viscoelastic nanofluids governed by fractional integrodifferential equations under Newtonian heating and thermal radiation, *Chin. J. Phys.*, **93** (2025), 584–600. https://doi.org/10.1016/j.cjph.2024.12.025

13. D. G. Prakasha, N. S. Malagi, P. Veeresha, B. C. Prasannakumara, An efficient computational technique for time-fractional Kaup-Kupershmidt equation, *Numer. Methods Partial Differ. Equations*, **37** (2021), 1299–1316. https://doi.org/10.1002/num.22580

14. P. Veeresha, D. G. Prakasha, N. Magesh, A. John Christopher, D. U. Sarwe, Solution for fractional potential KdV and Benjamin equations using the novel technique, *J. Ocean Eng. Sci.*, **6** (2021), 265–275. https://doi.org/10.1016/j.joes.2021.01.003

15. C. V. D. Kumar, D. G. Prakasha, N. B. Turki, Exploring the dynamics of fractional-order nonlinear dispersive wave system through homotopy technique, *Open Phys.*, **23** (2025), 20250128. https://doi.org/10.1515/phys-2025-0128

16. J. Xie, M. Wan, F. Zhao, J. Zhang, W. Shi, Dynamic perturbation analysis of fractional order differential quasiperiodic Mathieu equation, *Chaos*, **33** (2023), 123118. https://doi.org/10.1063/5.0163991

17. M. Shen, Z. Zhou, H. Chen, H. Fang, M. Zhang, A novel physically motivated Zener model for magnetohydrodynamics viscoelastic fluids with differential–integral fractional operator, *Phys. Fluids*, **37** (2025), 073128. https://doi.org/10.1063/5.0275223

18. Z. Mao, L. Feng, A. Xiao, F. Liu, I. Turner, Magnetohydrodynamic transient flow of dual-parameter fractional maxwell nanofluids past a vertical plate with generalised dual-phase-lagging heat conduction under ramped wall temperature conditions, *Eng. Comput.*, **42** (2026), 51. https://doi.org/10.1007/s00366-025-02267-0

19. A. Mehri, M. S. Abdo, H. Bouhadjera, A. Dawood, K. Aldwoah, R. Egami, Finite element analysis of a multi-term nonlinear time-fractional convection-diffusion equation with Caputo-Fabrizio derivative, *Boundary Value Probl.*, **2025** (2025), 1–26. https://doi.org/10.1186/s13661-025-02112-9

20. I. P. A. Papadopoulos, S. Olver, A sparse spectral method for fractional differential equations in one-spatial dimension, *Adv. Comput. Math.*, **50** (2024), 69. https://doi.org/10.1007/s10444-024-10164-1

21. J. C. Kalita, A. K. Dass, D. C. Dalal, A transformation-free HOC scheme for steady convection-diffusion on non-uniform grids, *Int. J. Numer. Methods Fluids*, **44** (2004), 33–53. https://doi.org/10.1002/fld.621

22. H. Wu, Y. He, G. Tang, W. Tao, Lattice Boltzmann simulation of flow in porous media on non-uniform grids, *Prog. Comput. Fluid Dyn.*, **5** (2005), 97–103. https://doi.org/10.1504/PCFD.2005.005821

23. J. Yang, Z. Xie, Z. Ji, H. Meng, Real-time heat transfer model based on variable non-uniform grid for dynamic control of continuous casting billets, *ISIJ Int.*, **54** (2014), 328–335. https://doi.org/10.2355/isijinternational.54.328

24. R. Webster, Algebraic multigrid and incompressible fluid flow, *Int. J. Numer. Methods Fluids*, **53** (2007), 669–690. https://doi.org/10.1002/fld.1297

25. L. Liu, G. Long, Z. Cen, A robust adaptive grid method for a nonlinear singularly perturbed differential equation with integral boundary condition, *Numer. Algorithms*, **83** (2020), 719–739. https://doi.org/10.1007/s11075-019-00700-2

26. G. Long, L. Liu, Z. Huang, Richardson extrapolation method on an adaptive grid for singularly perturbed Volterra integro-differential equations, *Numer. Funct. Anal. Optim.*, **42** (2021), 739–757. https://doi.org/10.1080/01630563.2021.1928698

27. A. Gupta, A. Kaushik, M. Sharma, A higher-order hybrid spline difference method on adaptive mesh for solving singularly perturbed parabolic reaction-diffusion problems with robin-boundary conditions, *Numer. Methods Partial Differ. Equations*, **39** (2023), 1220–1250. https://doi.org/10.1002/num.22931

28. L. Liu, Y. Liang, J. Zhang, X. Bao, A robust adaptive grid method for singularly perturbed Burger-Huxley equations, *Electron. Res. Arch.*, **28** (2020), 1439. https://doi.org/10.3934/era.2020076

29. Z. Mao, D. Luo, A robust adaptive grid method for first-order nonlinear singularly perturbed Fredholm integro-differential equations, *Networks Heterogen. Media*, **18** (2023), 1006–1023. https://doi.org/10.3934/nhm.2023044

30. L. Liu, Y. Liang, X. Bao, H. Fang, An efficient adaptive grid method for a system of singularly perturbed convection-diffusion problems with Robin boundary conditions, *Adv. Differ. Equ.*, **2021** (2021), 1–13. https://doi.org/10.1186/s13662-020-03166-y

31. M. Sheikholeslami, A. Ghasemi, Solidification heat transfer of nanofluid in existence of thermal radiation by means of FEM, *Int. J. Heat Mass Transfer.*, **123** (2018), 418–431. https://doi.org/10.1016/j.ijheatmasstransfer.2018.02.095

32. E. Abu-Nada, Application of nanofluids for heat transfer enhancement of separated flows encountered in a backward facing step, *Int. J. Heat Fluid Flow*, **29** (2008), 242–249. https://doi.org/10.1016/j.ijheatfluidflow.2007.07.001

33. B. Jin, Fractional calculus, in *Fractional Differential Equations*, Springer, Cham, (2021), 19–58. https://doi.org/10.1007/978-3-030-76043-4

34. H. Schiessel, C. Friedrich, A. Blumen, Fractional powers of infinitesimal generators of semigroups, in *Applications of Fractional Calculus in Physics (Ed. R. Hilfer)*, World scientific, Singapore, (2000), 131–170. https://doi.org/10.1142/9789812817747

35. H. Schiessel, R. Metzler, A. Blumen, T. F. Nonnenmacher, Generalized viscoelastic models: Their fractional equations with solutions, *J. Phys. A: Math. Gen.*, **28** (1995), 6567. https://doi.org/10.1088/0305-4470/28/23/012

36. C. Friedrich, Relaxation and retardation functions of the maxwell model with fractional derivatives, *Rheol. Acta*, **30** (1991), 151–158. https://doi.org/10.1007/BF01134604

37. W. Tan, W. Pan, M. Xu, A note on unsteady flows of a viscoelastic fluid with the fractional Maxwell model between two parallel plates, *Int. J. Nonlinear Mech.*, **38** (2003), 645–650. https://doi.org/10.1016/S0020-7462(01)00121-4

38. M. Shen, L. Chen, M. Zhang, F. Liu, A renovated Buongiorno's model for unsteady Sisko nanofluid with fractional Cattaneo heat flux, *Int. J. Heat Mass Transfer.*, **126** (2018), 277–286. https://doi.org/10.1016/j.ijheatmasstransfer.2018.05.131

39. M. A. Ezzat, Thermoelectric MHD non-Newtonian fluid with fractional derivative heat transfer, *Phys. B*, **405** (2010), 4188–4194. https://doi.org/10.1016/j.physb.2010.07.009

40. Z. Wang, S. Vong, Compact difference schemes for the modified anomalous fractional sub-diffusion equation and the fractional diffusion-wave equation, *J. Comput. Phys.*, **277** (2014), 1–15. https://doi.org/10.1016/j.jcp.2014.08.012

41. M. Stynes, E. O'Riordan, J. L. Gracia, Error analysis of a finite difference method on graded meshes for a time-fractional diffusion equation, *SIAM J. Numer. Anal.*, **55** (2017), 1057–1079. https://doi.org/10.1137/16M1082329

42. P. Roul, A robust adaptive moving mesh technique for a time-fractional reaction-diffusion model, *Commun. Nonlinear Sci. Numer. Simul.*, **109** (2022), 106290. https://doi.org/10.1016/j.cnsns.2022.106290

43. J. Huang, Z. Cen, J. Zhao, An adaptive moving mesh method for a time-fractional Black–Scholes equation, *Adv. Differ. Equ.*, **2019** (2019), 516. https://doi.org/10.1186/s13662-019-2453-1

44. Z. Cen, L. Liu, A. Xu, A second-order adaptive grid method for a nonlinear singularly perturbed problem with an integral boundary condition, *J. Comput. Appl. Math.*, **385** (2021), 113205. https://doi.org/10.1016/j.cam.2020.113205

45. M. Cakir, Y. Ekinci, E. Cimen, A numerical approach for solving nonlinear Fredholm integro-differential equation with boundary layer, *Comput. Appl. Math.*, **41** (2022), 259. https://doi.org/10.1007/s40314-022-01933-z

46. M. Cakir, B. Gunes, A fitted operator finite difference approximation for singularly perturbed Volterra–Fredholm integro-differential equations, *Mathematics*, **10** (2022), 3560. https://doi.org/10.3390/math10193560

47. S. Priyadarshana, A. Padhan, J. Mohapatra, Adaptive grid based moving mesh algorithms for singularly perturbed second-order Volterra integro differential equations, *Quaest. Math.*, **48** (2024), 1007–1028. https://doi.org/10.2989/16073606.2025.2462939

48. N. Kopteva, M. Stynes, A robust adaptive method for a quasilinear one-dimensional convection-diffusion problem, *SIAM J. Numer. Anal.*, **39** (2001), 1446–1467. https://doi.org/10.1137/S003614290138471X

49. W. S. Manebo, M. M. Woldaregay, T. G. Dinka, G. F. Duressa, A computational approach to solving a second-order singularly perturbed Fredholm integro-differential equation with discontinuous source term, *Numer. Algor.*, **97** (2024), 1415–1430. https://doi.org/10.1007/s11075-024-01756-5

50. S. Jiang, J. Zhang, Q. Zhang, Z. Zhang, Fast evaluation of the Caputo fractional derivative and its applications to fractional diffusion equations, *Commun. Comput. Phys.*, **21** (2015), 650–678. https://doi.org/10.4208/cicp.OA-2016-0136

51. X. Gu, S. Wu, A parallel-in-time iterative algorithm for Volterra partial integro-differential problems with weakly singular kernel, *J. Comput. Phys.*, **417** (2020), 109576. https://doi.org/10.1016/j.jcp.2020.109576

52. J. Buongiorno, Convective transport in nanofluids, *J. Heat Transfer*, **128** (2006), 240–250. https://doi.org/10.1115/1.2150834

53. F. Mebarek-Oudina, Preeti, A. S. Sabu, H. Vaidya, R. W. Lewis, S. Areekara, et al., Hydromagnetic flow of magnetite-water nanofluid utilizing adapted Buongiorno model, *Int. J. Mod. Phys. B*, **38** (2024), 2450003. https://doi.org/10.1142/S0217979224500036

AIMS Press